Research Article | Vol. 28, No. 8 / 13 April 2020 / Optics Express 11597
Optics EXPRESS

Simplified retrieval method for Edge Illumination X-ray phase contrast imaging allowing multi-modal imaging with fewer input frames

IAN BUCHANAN,[1,*] ALBERTO MITTONE,[2,3] ALBERTO BRAVIN,[2] PAUL DIEMOZ,[1] MARCO ENDRIZZI,[1] AND ALESSANDRO OLIVO[1]

[1]*Department of Medical Physics and Biomedical Engineering, University College London, Gower Street, WC1E 6BT London, UK*
[2]*European Synchrotron Radiation Facility, 38043 Grenoble, France*
[3]*CELLS - ALBA synchrotron light source, Carrer de la Llum, 2-26, 08290 Cerdanyola del Valles, Barcelona, Spain*
[*]*ian.buchanan.15@ucl.ac.uk*

Abstract: We present data from an implementation of Edge Illumination (EI) that uses a detector aperture designed for increasing dynamic range, suitable for clinically relevant X-ray energies and demonstrated here using synchrotron radiation. By utilising a sufficiently large crosstalk between pixels, this implementation enables single-scan imaging for phase and absorption, and double-scan for phase, absorption and dark field imaging. The presence of the detector mask enables a direct comparison between conventional EI and beam tracking (BT), which we conduct through Monte Carlo and analytical modelling in the case of a single-scan being used for the retrieval of all three contrasts. In the present case, where the X-ray beam width is comparable to the pixel size, we provide an analysis on best-positioning of the beam on the detector for accurate signal retrieval. Further, we demonstrate an application of this method by distinguishing different concentrations of microbubbles via their dark field signals at high energy using an EI system.

1. Introduction

X-ray phase contrast imaging (XPCi) has continuously seen research pursuing applications which benefit from low dose [1–5]. This can be achieved by either reducing the time for which samples are exposed to X-rays, or, within limits, increasing the X-ray energy [1], which has the added benefit of increasing the penetration depth of photons. In the former case, noise can become an obstacle to image quality and in the latter case, contrast is typically decreased.

XPCi has the potential to overcome this limitation, since the parameter responsible for phase contrast decreases approximately with the square of photon energy, E^{-2}, whereas that responsible for conventional transmission imaging contrast fall as $E^{-3.5-3.6}$ [6], depending on the energy range. These parameters are expressed by an object's complex refractive index, $n = 1 - \delta + i\beta$, with β in some materials being up to three orders of magnitude smaller than δ.

While EI, in general, has a resolution limit determined by the system parameters such as the source and aperture sizes employed [7], structures on a scale below this limit generate so-called "dark field" contrast. This contrast is not resolvable per se, rather it is an indication of the presence of microstructures within a sample and is due to a distribution of refraction angles within the X-ray beam [8]. Dark field signals can be caused by, for example, micro-damage in carbon-reinforced polymers [9], or microbubbles [8,10,11], the latter of which has been considered as a possible XPCi contrast agent in clinical and pre-clinical settings, and is used in this work.

#372312 https://doi.org/10.1364/OE.372312
Journal © 2020 Received 11 Jul 2019; revised 13 Feb 2020; accepted 28 Feb 2020; published 6 Apr 2020

Optics EXPRESS

In EI, dark field contrast can either be directly measured at the cost of dose-efficiency [12] (where most of the primary beam is discarded), or can be retrieved through the processing of multiple image acquisitions [13]. With an assumption of sample homogeneity, it is possible to retrieve quantitative parameters about the sample (typically thickness) with a single sample image [14,15]. In circumstances where individual beams are larger than the pixels being employed, such that they may be well resolved [16,17], it is also possible to separate the sample properties into attenuation, phase and scattering maps with a single image frame. Since small pixel sizes often mean low efficiency, especially at high x-ray energies, implementation of such techniques with larger, more efficient pixels, would avoid losing any advantages in dose reduction being employed. Other XPCi methods, such as grating interferometry (GI), analyzer-based imaging (ABI), or Shack-Hartmann imaging, are also capable of extracting attenuation, phase and scattering maps [18–20], though with differing conditions on system length or detector resolution, optical elements, processing methods [21–24]. Concerning Fourier methods of signal retrieval, Vittoria *et al* [16] showed that the use of these methods with polychromatic beams, and in the presence of pixel crosstalk, may lead to an underestimation of absorption signals and produce spurious dark field signals. While GI and ABI have broadly been applied in various settings, their use is reliant upon spatially coherent or monochromatic X-rays respectively, with a more thorough discussion of the systems' requirements made available by Diemoz *et al* [25].

In this work, we present an implementation of EI whereby samples are scanned once across a narrow transmitting aperture to enable quantitative phase and transmission retrieval with no assumptions of sample homogeneity and loose restrictions on pixel size and crosstalk. In fact, crosstalk is used to overcome previous requirements of the beam being larger than the pixel, which necessitates the use of high resolution detectors and ultimately limits the field of view. Within the same experimental framework, we compare the data retrieved in this case with those from conventional double and triple-scan EI retrieval methods, and demonstrate the ability to retrieve all of the contrasts mentioned using only two image acquisitions instead of three. Finally, we show through Monte Carlo and analytical modelling, a comparison between this retrieval and that used in beam-tracking [26] for single-frame retrieval of all three signals, in the yet unexplored case of the beam size being approximately equal to that of the pixel.

We found this imaging format to be simple and fast, and envisage its use for extending the large dose reduction demonstrated by Diemoz *et al* [1] to more complex samples while also allowing for quantitative separation of phase, absorption and dark field. The relatively large pixel size, compared to the beam width, also indicates that large fields of view may be employable in the future with this method, particularly with multi-aperture systems [26,27], as the number of pixels in a detector is typically limited to a few thousands.

2. Methods

The experimental data presented in this paper were collected at the European Synchrotron Radiation Facility (ESRF) beamline ID17, at an energy of 50 keV monochromatized by a double-bent Laue crystal [28].

With the source located at approximately 150 m from the detector, a modified Edge Illumination system was implemented by placing a pre-sample mask, M1, 2.5 m from the detector and a detector mask, M2, itself 0.5 m from the detector. The detector was a PCO.Edge (type 5.5) camera [29], coupled with a 0.3× optics and a 50 um thick GADOX scintillator screen, leading to a final pixel size of 21.6 μm. Before the introduction of a sample, an ion chamber (0.125 cm^3 semiflex tube chamber, Model 31002; PTW-Freiburg, Freiburg im Breisgau, Germany) was placed in the sample position - downstream of M1 - to measure the air kerma. The chamber, calibrated at the National Metrology Institute of Germany (Physikalisch-Technische Bundesanstalt, Braunschweig, Germany), was connected to the universal dosemeter module (UNIDOS; PTW-Freiburg) and the measurement protocol followed the procedure described by Mittone *et al* [30].

Optics EXPRESS

Both masks consist of periodic free-standing tungsten septa, approximately 1 mm thick, with apertures of 20 μm and 100 μm in M1 and M2 respectively, and approximately equal pitches of 450 μm. The aperture of M1 narrows the beam, which then scans the aperture of the detector mask as M1 is translated perpendicularly to the beam - see Fig. 1(a). The “local" (individual pixel) intensities recorded during this translation form the illumination curve (IC) functions, which are averaged to produce the “global" IC, seen in Fig. 1(b). ICs determine the sensitivity of the system to phase effects [31] and in most previous EI studies, different positions of M1 are used in separate scans to obtain independent results from the sample, while the use of local ICs here reduces the need for separate positions of M1.

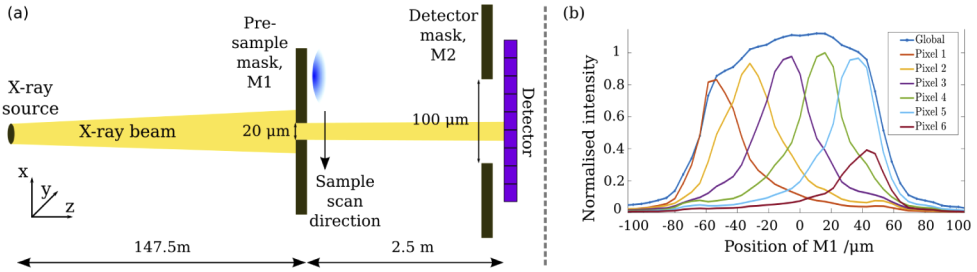

Fig. 1. (a) Schematic diagram of the EI setup used at the ESRF (not to scale). (b) Intensity profiles (Illumination Curves; ICs), normalised to appear on the same scale, acquired by scanning the pre-sample mask, M1, across an aperture on the detector mask, M2. Pixel 6 has a lower peak intensity as it is almost entirely an effect of crosstalk; the pixel itself is mostly obstructed by M2.

The design intent of M2’s aperture being 5× greater than the apertures in M1 was to ensure that all refracted X-rays were collected, thus achieving a high dynamic range when integrating all photons captured by one aperture of M2, as implemented by Diemoz *et al.* [1]. This extended aperture also opens the possibility of considering data acquired by individual pixels in relation to their unique ICs. In this case, if the ICs are overlapping and sufficiently spaced, as seen in Fig. 1(b), a single image of a sample may constitute multiple measurements of the effect it has on the beam while in the edge illumination condition.

The samples imaged were chosen to exhibit absorption, phase and dark field contrast in various combinations. They were a Nylon-6 wire, of radius 500 μm, and varying Expancel microsphere concentrations - with a known size distribution, shown in Fig. 2(a) - suspended in an ultrasound gel.

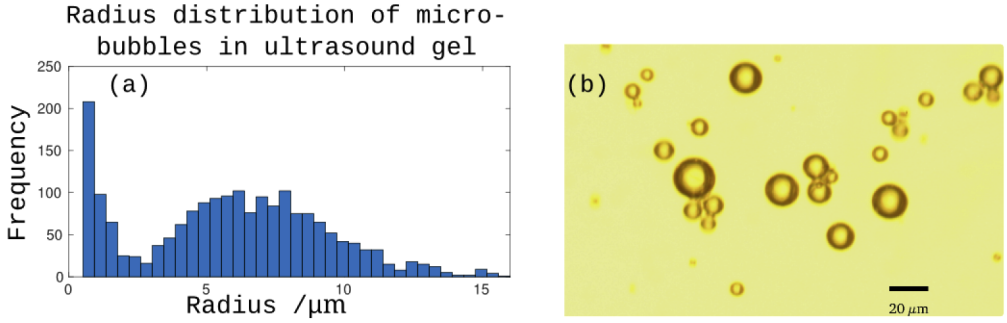

Fig. 2. (a) Measured size distribution of microspheres; (b) Example image displaying 20× optical magnification of Expancel microspheres.

Optics EXPRESS

2.1. Scattering sample preparations

Expancel microspheres consist of polymer shells, filled with isobutane gas. The shell is rigid unless subjected to large changes in temperature or pressure and the thickness is negligible compared to the sphere radius, making them ideal for stable imaging tests. The highest concentration of spheres in ultrasound gel - ≈2.3% by volume - was produced in a large quantity, with ultrasound gel being chosen as the solvent to prevent the microspheres from floating or bursting [11].

The samples were optically imaged with a 20× magnification in a grid formation, acquiring more than 200 images, an example of which is shown in Fig. 2(b). From these, the concentration and size distribution of microbubbles in the gel was determined. Lower concentrations of spheres were made by diluting this stock concentration with known amounts of water, making relative microbubble concentrations of 1/2 and 1/3. These were then pipetted into 1 cm wide cuvettes for imaging.

2.2. Experimental procedure and retrieval

By scanning M1 over one period and integrating the intensities of each pixel in the detector aperture, we obtained the global IC. In Fig. 1(b), underneath the global IC, the individual pixel intensities are also plotted, with the global and local ICs being normalised such that they appear on the same scale. In either case, any effects due to a sample are treated as operators on these curves, e.g. multiplication by a scalar (transmission), rigid shifts (refraction) or broadening of the beam by convolution with a function (dark field). We express the above via the equation [32]:

$$I_{\text{detector}} = t \times (L * O(s))(x_{\text{M1}} - r), \tag{1}$$

where t is the object transmission, L is the IC, $*$ is the convolution operator, $O(s)$ is the sample scattering function with some width parameter, s, x_{M1} is the position of M1 with respect to the centre of M2's aperture and $r = -\Delta\theta_R z_{od}$ is the effective shift of the beamlet due to the sample induced refraction at a distance z_{od} from the detector. L was finely sampled and fitted, in both the global and individual pixel IC cases, with smoothing splines.

For the retrieval of these signals in the reduced frame cases, local pixel ICs were convolved with a sample function as in Eq. 1, and for the multi-frame cases, the global ICs were used. The scattering function, in the case of the wire sample, was assumed to be a Dirac delta, while a Gaussian distribution was assumed for the different microbubble concentrations. Trial parameters of t, r, and s used in the retrieval converge towards the true sample values through a least-squares minimisation process that compares interpolated data predicted by Eq. 1, for the IC sampling points specified, against the measured data.

For the wire sample, data was acquired while M1 was positioned at ±49.5 μm, as marked in Fig. 3(a). For the scattering samples, M1 was positioned at −53.0 μm; −34.5 μm and 41.0 μm. The wire sample was scanned in 10μm steps with an exposure time of 190ms per step (≈10mGy entrance dose) and the scattering samples in 20 μm steps with an exposure time of 100ms per step (≈5mGy). As each sample was exposed uniformly to some amount of radiation, the overall entrance dose values and exposure times were 20 mGy over 19 s for the wire sample, which was double-exposed due to the half-aperture step size, and 5 mGy over 50 s for the scattering samples.

2.3. Determining optimal beam sampling positions in EI and beam tracking

Theoretical studies of the retrieval algorithm developed here, and of the beam-properties analysis used in BT, were developed to determine which position of M1 yields best results and how, if at all, this is affected by variations in pixel response across the aperture of M2. This was achieved by tracking the retrieval algorithms' accuracy as a function of x_{M1} for varying levels of noise. First, a set of seven finely sampled, local ICs were obtained using the Monte Carlo simulation outlined

Optics EXPRESS

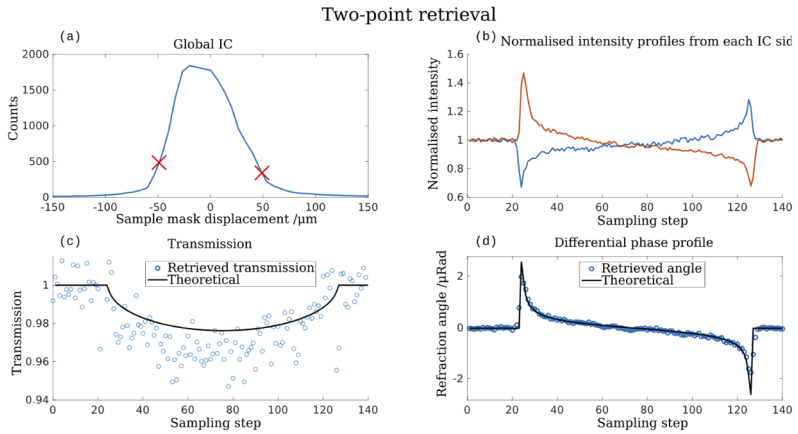

Fig. 3. Two-point retrieval of the Nylon-6 wire. (a) is the global IC, marked with the sampling points used; (b) displays the raw data profiles. Retrieved and theoretical profiles for transmission and refraction signals are shown in (c) and (d), respectively.

below; these IC functions were modified to account for the presence of various samples, as in equation 1. A succession of different sample parameters were used, randomly setting absorption between 0% and 3%, refraction angle between -5 μrad and 5 μrad, and scattering signal between 0 and 5 μm^2. For each sampling position, the vector of pixel intensities was used as input to the retrieval. The resulting difference between the fitted parameters and the true values was tracked for various positions of M1. This was repeated for the beam tracking case, where the detector mask, M2, was removed and the beam profile sampled by translating M1 in the same way as before.

Noise was modelled by multiplying the sample data vector (one value for each pixel, with seven in total) by a vector that took the form of $((1-a)+2a\times \texttt{rand}(7,1))$, where a was close to zero, and `rand` is a uniform distribution function that returns values between 0 and 1. For each sampling position, the noise vector was generated ten times per value of a and if the retrieval performed well, the value of a was increased and the sampling points retested.

The retrieval performance was quantified by dividing the percentage deviation between true and retrieved scattering parameters, then dividing by the precision such that the best performing positions scored highly. The retrieved transmission and refraction parameters were not used in the performance analysis as their retrieval accuracy was consistent for all the points tested. All data were processed in MATLAB.

2.4. *Monte Carlo model for single-frame retrieval and beam tracking comparison*

To continue exploring options that may enable a further reduction of the required number of frames, an identical experimental setup was coded using the Monte Carlo engine, McXtrace [33], adapted for EI use by Millard *et al* [34].

Each mask was modelled as a three dimensional pair of absorbing septa, 1 mm in depth, with 20 μm and 100 μm separation for sample and detector mask, respectively. A 50 keV source was placed 148 m from M1 and incident upon a detector grid whose pixels are equivalent to those of the PCO.Edge. Before placing a sample, local ICs of the detection system were simulated by scanning M1 over a single period. For the comparison with BT retrieval methods, the detector mask was removed and the beam profile was sampled by scanning M1 over one pixel width instead of the mask period. The retrieval mechanism in this case is the same, except pixels are assumed to have identical response functions and the IC is replaced by the beam profile.

Optics EXPRESS

A three dimensional sphere-map was generated in MATLAB and exported to a text file for reading by McXtrace, where the microspheres were modelled as being immersed in a cylinder of water. They had a volume density of 2.5% (approximately 10^8 microspheres / ml) and a size distribution as seen in Fig. 2(a). Upon entering the sample region, X-rays check for intersections with spheres using coordinates and radii in the sphere map. Snell's law is used to model the refraction event at the boundaries of each sphere, whose refractive index was that of acrylonitride, as described by the NIST database and chosen as a representative polymer for the microspheres' shell.

The effect of the detector point-spread function, being larger than the individual pixels due to light spreading in the scintillator, was included by convolving raw data with a Lorentzian curve of width parameter 0.8 pixels, chosen as it lead to a good match between simulated and measured ICs.

The sample component was scanned across M1's aperture in steps of 10.8 μm, with each step using 1.5×10^7 50 keV photons (roughly 3300 photons per pixel), approximately corresponding to an integration time of 150ms.

3. Results

Figures 3 and 4 show outputs of the two and single-frame Nylon wire retrievals, respectively. The same format is used in each figure, with (a) showing the IC and sampling positions of M1 used in the object scan; (b) showing the normalised intensity inputs, obtained by averaging the wire image over ten vertical pixels, and (c) and (d) showing the transmission and refraction-angle retrieved wire profiles respectively. The final two plots use the same y axis for ease of comparison and also, superimposed on the plots, are the wire's theoretical transmission and refraction profiles, showing good agreement in both cases. Of note is that only half the data set of Fig. 3 was used to obtain the results of Fig. 4, with the single-frame retrieved transmission channel also being 40% less noisy than the two-frame equivalent due to the greater number of inputs used in the single-frame retrieval.

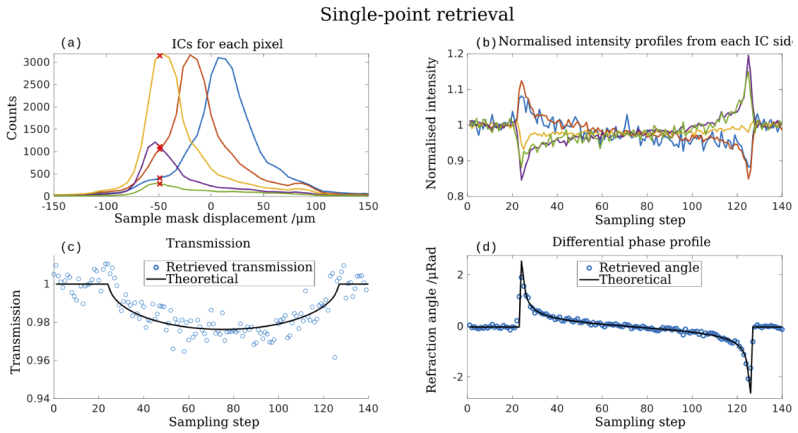

Fig. 4. Single-point retrieval of the Nylon-6 wire. (a) displays the individual pixel ICs, marked with the single sampling point used; (b) shows the normalised raw data profiles. Retrieved and theoretical profiles for transmission and refraction angle of the beam are shown in (c) and (d), respectively.

For retrieval of the scattering samples, the same approach was taken. Three M1 acquisition points were needed for an effective retrieval using the global IC, whereas only the two inner M1 positions, -34.5 μm and 41.0 μm, were needed to retrieve the same quantitative values

Optics EXPRESS

for transmission, refraction and scattering signal strength when considering the pixel-resolved data. Results obtained with this procedure for the different concentrations of microspheres are illustrated in Fig. 5. The plots show a good discrimination of different sphere concentrations in the dark field and poor discrimination in transmission. As retrieval of dark field contrast can be highly sensitive to noise, the low precision of scattering data is particularly visible in the two-frame retrieval, where the associated noise for each signal, of which there are five for each of the two sampling positions, is large as compared to the “three-frame" method, where averaging of pixel values reduces the noise for each input. The two-frame retrieval was also disadvantaged by using non-ideal IC sampling positions, which is discussed below.

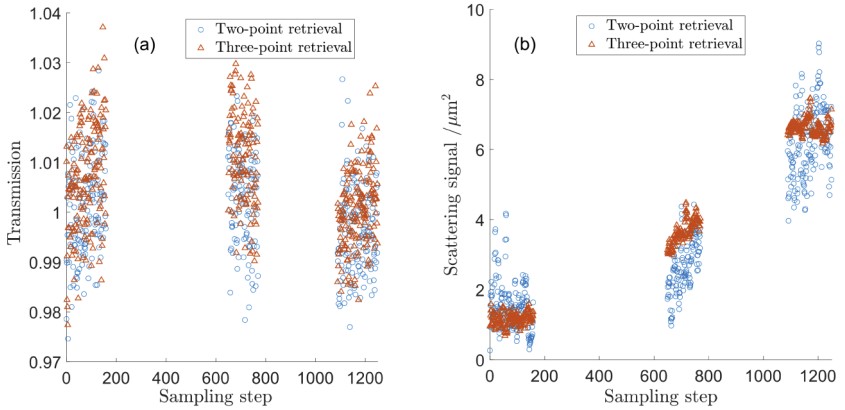

Fig. 5. Retrieved parameters for scattering samples as acquired from the local, two-point retrieval and the global, three-point retrieval. (a) shows transmission through the samples and (b), the scattering signals. The relative microbubble concentrations are 1/3, 1/2 and 1 (see text), from left to right. Gaps between data groups skip the edges of cuvettes used.

Figure 6(a) displays the approach used in determining the optimal sampling position as described in 2.4, with (b) showing the results. Even before adding noise, it was seen that the scattering signal was only retrieved accurately when the sampling was near a local IC peak, while transmission and refraction were relatively stable for most positions of M1. As noise

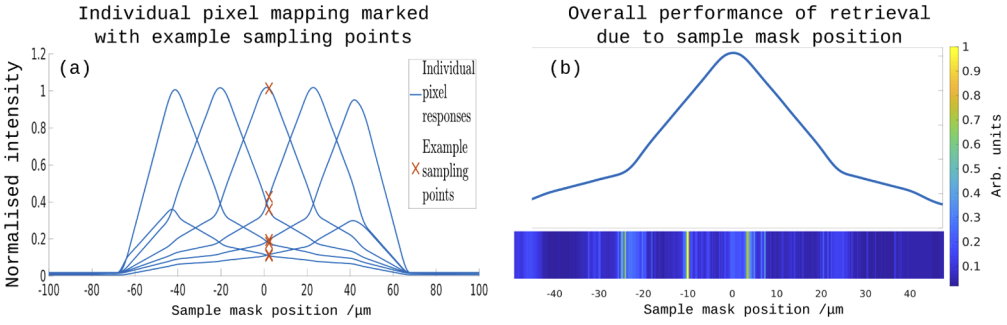

Fig. 6. Testing of retrieval algorithm accuracy under single-scan conditions for different positions of M1 and increasing levels of noise. (a) displays the individual ICs for each pixel, with an example sampling vector marked; (b) considers the centre pixel’s IC, with the heat-map corresponding to the retrieval’s performance quality (quantified by dividing the accuracy of the retrieval by its precision in the case of high noise) as a function of x_{M1} and normalised by the best performing position.

Optics EXPRESS

increased, $x_{M1} = 2.3$ μm led to the minimum difference between the retrieved and true scattering parameters, as demonstrated by the heat-map in Fig. 6(b).

The viability of single-frame retrieval was then investigated through Monte Carlo simulations, using this position of M1, with the results shown in Fig. 7, which displays retrieved transmission, refraction angles and scattering signal from the single-frame Monte Carlo simulation outlined in section 2.4. The region containing microbubbles extends ±150 μm in the vertical direction around the centre of the simulated phantom and the boundaries of this signal are clear in Fig. 7(c), confirming that the microbubbles, and not the water surrounding them, are responsible for generating the dark field contrast. In the refraction-retrieved image, the texture seen within the phantom is due to the small number of microspheres that are large enough to be resolvable, or due to microbubbles whose edges are overlapping in the z direction, such that they produce spurious refraction signals.

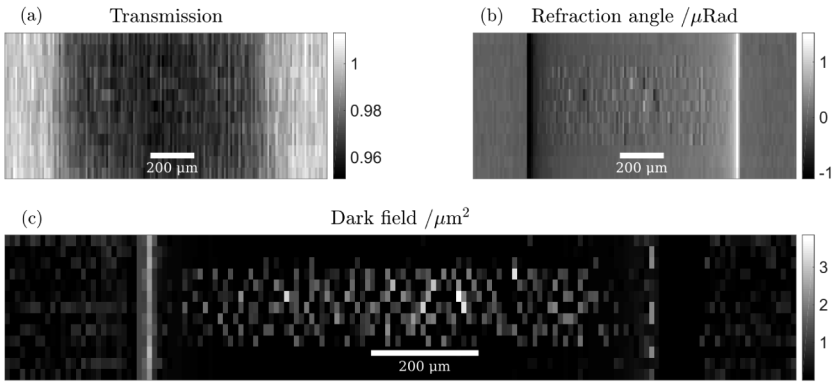

Fig. 7. Single scan retrieval, from simulated data, of transmission (a), refraction angle (b) and dark field signals (c) at 50 keV. The simulated object is a water cylinder of radius 550 μm, with a 2.5% volume concentration of microspheres in the central region.

Lastly, to compare this local IC retrieval method with the algorithm used in beam tracking, where a curve representing the beam profile (often a Gaussian, but in this case a Lorentzian) is used, Fig. 8(a) shows the conceptually different retrieval approach - where the pixel data is treated as an ensemble measurement of the beam - and (b) displays the optimal sampling positions as

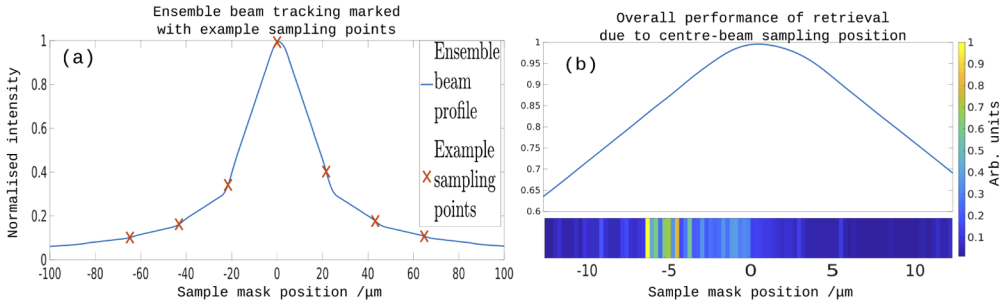

Fig. 8. Using the same setup without the detector mask, M2, the beam-tracking implementation is examined in terms of accuracy for retrieved values in the case of an X-ray beam whose width is comparable to pixel size. (a) displays the beam profile on the detector marked with an example sampling vector corresponding to each pixel position; (b) displays the retrieval performance quality (the accuracy of the retrieval divided by its precision in the case of high-noise) via the heat-map as a function of the centre-beam sampling position.

Optics EXPRESS

determined by the same method described in 2.4. The best scoring position here was normalised to one, as in Fig. 6, with the relative quantitative accuracy between these methods being nearly equal.

4. Discussion

The EI implementation used here has likenesses to that employed by Diemoz *et al.* [1], the key differences being the lower x-ray energy employed, chosen in part for its clinical relevance - 50 keV is the effective energy of a 100 kVp tungsten anode beam filtered by 300 μm of copper, which may be used for chest radiography [35] - and the use of smaller pixels, though still slightly greater than the width of the beamlet. This latter property enables the development of a retrieval method that bears similarities with that used in beam-tracking [26] and, to some extent, that used in conjunction with asymmetric mask implementations [36]. The presence of the detector mask here allows for direct comparisons between EI and beam tracking without needing to fully resolve the beam, instead making use of detector crosstalk to create multiple ICs with distinct sampling points.

Retrieved image quality and quantitative accuracy for single-frame absorption and phase retrieval is seen to be on a par with the conventional two-frame approach, as shown by Figs. 3 and 4, while the nature of the retrieval places no restrictive assumptions on sample homogeneity and provides direct access to the refraction angle.

Dark field signal can be retrieved using fewer than three acquisitions and this simplified approach shows good agreement with the conventional three-point retrieval. However, this method shows higher sensitivity to noise and positioning of the pre-sample mask, as evidenced by the wider spread of retrieved dark field signal in Fig. 5. In the single-frame case, the sensitivity to noise is further explored in Fig. 6, where it was found that noise of up to 2.5% - as defined above - led to a quantitative accuracy of approximately 25% for dark field contrasts when M1 was fully aligned with M2, meaning that roughly 2500 counts per pixel (if Poisson statistics are assumed) would be required for this level of accuracy.

Figure 6 indicates that the optimal sampling position of M1 for single-frame retrieval is far from the detector mask edges, meaning that no fraction of the beam gets absorbed by the mask septa after having traversed the sample, and no dose is deposited unnecessarily to the sample. With M1 in this position, the setup can also be compared to that of beam tracking - in the special case where the beam width is approximately equal to the pixel size. Figure 8 shows how the accuracy and precision of the beam tracking retrieval algorithm described by Vittoria *et al.* [26], which uses a fitted curve to describe the beam profile, varies with the position of M1 or, in other words: how the sampling of the crosstalk-smeared beam affects the retrieval performance. Perhaps unsurprisingly, the best position for sampling with this algorithm is also in the region of $x_{\mathrm{M1}} = 2.3$ μm, which yields a similar accuracy of approximately 25% at the same noise threshold as above. Both Figs. 6 and 8 suggest that precise positioning of M1 is necessary when undertaking single-frame retrievals.

As EI is a non-interferometric [37], achromatic [32] technique, it is expected that this approach could be translated to a lab setting where polychromatic extended sources are used. Indeed, an extended source would have a similar effect as crosstalk between pixels on the individual pixel ICs described here. Additionally, it should be possible to use multiple apertures - common in lab-based EI schemes - that allow access to larger fields of view than used here. Where resolution higher than the pre-sample mask pitch is required, this could be obtained through sample dithering, which in this scenario would require translation of the sample only through a distance equal to the pitch of M1, rather than the sample's own width, thus eliminating the need for full sample scanning.

It is worth emphasising that this technique benefits from the presence of some degree of crosstalk between pixels and in particular, crosstalk with long "tails". Without such an effect,

Optics EXPRESS

the individual pixel ICs would be narrower; should this eliminate their overlap, the possibility to multi-sample ICs for any single position of M1 would be diminished due to the increased relevance of noise, and the retrieval approach would become unfeasible.

5. Conclusion

We have demonstrated an implementation of EI XPCi which allows for direct comparison between high-dynamic range EI and beam-tracking functionalities, enabling single-frame transmission, phase and dark field retrieval. This retrieval approach utilises crosstalk between pixels to form regularly spaced, separate IC functions within a detector mask aperture. Data from these pixels represent complementary sampling points along separate ICs and may hence be used to numerically separate the transmission, average refraction angle and dark field signals. Through iterative testing of the retrieval algorithm, it was found that the optimal position of the pre-sample mask was also the most dose-efficient (the central point of the global IC). This was compared to a beam-tracking equivalent of the experimental setup, which showed that the two methods produce consistent results, with similar constraints on where each pixel samples the beam. We have also shown the capability of EI to detect and distinguish between dark field signals due to varying concentrations of microspheres at high energy. It is envisaged that the EI implementation presented here could work with polychromatic, extended sources and would be useful for pre-clinical and biological imaging purposes, where the presence of bone or any sample inhomogeneities can hinder the use of other single-frame retrieval methods.

Funding

Engineering and Physical Sciences Research Council (EP/M507581/1); Vetenskapsrådet (X2015-99x-22731-01-4); Royal Academy of Engineering (Research Fellowships scheme, ME, and Chairs in Emerging Technology scheme, AO).

Acknowledgments

The authors would like to thank Gibril Kallon for useful discussions, and Barbara Dymerska for providing a MATLAB script to quantify microbubble concentrations.

Disclosures

The authors declare that there are no conflicts of interest related to this article.

References

1. P. C. Diemoz, A. Bravin, A. Sztrókay-Gaul, M. Ruat, S. Grandl, D. Mayr, S. Auweter, A. Mittone, E. Brun, C. Ponchut, M. F. Reiser, P. Coan, and A. Olivo, "A method for high-energy, low-dose mammography using edge illumination x-ray phase-contrast imaging," Phys. Med. Biol. **61**(24), 8750–8761 (2016).
2. C. K. Hagen, P. R. T. Munro, M. Endrizzi, P. C. Diemoz, and A. Olivo, "Low-dose phase contrast tomography with conventional x-ray sources," Med. Phys. **41**(7), 070701 (2014).
3. A. Astolfo, M. Endrizzi, F. A. Vittoria, P. C. Diemoz, B. Price, I. Haig, and A. Olivo, "Large field of view, fast and low dose multimodal phase-contrast imaging at high x-ray energy," Sci. Rep. **7**(1), 2187 (2017).
4. A. Mittone, A. Bravin, and P. Coan, "Low-dose quantitative phase contrast medical CT," Meas. Sci. Technol. **29**(2), 024006 (2018).
5. M. J. Kitchen, G. A. Buckley, T. E. Gureyev, M. J. Wallace, N. Andres-Thio, K. Uesugi, N. Yagi, and S. B. Hooper, "CT dose reduction factors in the thousands using x-ray phase contrast," Sci. Rep. **7**(1), 15953 (2017).
6. D. Paganin, *Coherent X-Ray Optics* (Oxford University, 2006).
7. P. C. Diemoz, F. A. Vittoria, and A. Olivo, "Spatial resolution of edge illumination x-ray phase-contrast imaging," Opt. Express **22**(13), 15514 (2014).
8. L. Rigon, F. Arfelli, and R. H. Menk, "Three-image diffraction enhanced imaging algorithm to extract absorption, refraction, and ultrasmall-angle scattering," Appl. Phys. Lett. **90**(11), 114102 (2007).
9. D. Shoukroun, L. Massimi, F. Iacoviello, M. Endrizzi, D. Bate, A. Olivo, and P. Fromme, "Enhanced composite plate impact damage detection and characterisation using x-ray refraction and scattering contrast combined with ultrasonic imaging," Composites, Part B **181**, 107579 (2020).

Optics EXPRESS

10. F. Arfelli, L. Rigon, and R. H. Menk, "Microbubbles as x-ray scattering contrast agents using analyzer-based imaging," Phys. Med. Biol. **55**(6), 1643–1658 (2010).
11. T. P. Millard, M. Endrizzi, L. Rigon, F. Arfelli, R. H. Menk, J. Owen, E. Stride, and A. Olivo, "Quantification of microbubble concentration through x-ray phase contrast imaging," Appl. Phys. Lett. **103**(11), 114105 (2013).
12. T. P. Millard, M. Endrizzi, N. Everdell, L. Rigon, F. Arfelli, R. H. Menk, E. Stride, and A. Olivo, "Evaluation of microbubble contrast agents for dynamic imaging with x-ray phase contrast," Sci. Rep. **5**(1), 12509 (2015).
13. M. Endrizzi, P. C. Diemoz, T. P. Millard, J. Louise Jones, R. D. Speller, I. K. Robinson, and A. Olivo, "Hard X-ray dark-field imaging with incoherent sample illumination," Appl. Phys. Lett. **104**(2), 024106 (2014).
14. D. Paganin, S. C. Mayo, T. E. Gureyev, P. R. Miller, and S. W. Wilkins, "Simultaneous phase and amplitude extraction from a single defocused image of a homogeneous object," J. Microsc. **206**(1), 33–40 (2002).
15. P. C. Diemoz, F. A. Vittoria, C. K. Hagen, M. Endrizzi, P. Coan, E. Brun, U. H. Wagner, C. Rau, I. K. Robinson, A. Bravin, and A. Olivo, "Single-image phase retrieval using an edge illumination X-ray phase-contrast imaging setup," J. Synchrotron Radiat. **22**(4), 1072–1077 (2015).
16. F. A. Vittoria, M. Endrizzi, P. C. Diemoz, U. H. Wagner, C. Rau, I. K. Robinson, and A. Olivo, "Virtual edge illumination and one dimensional beam tracking for absorption, refraction, and scattering retrieval," Appl. Phys. Lett. **104**(13), 134102 (2014).
17. H. H. Wen, E. E. Bennett, R. Kopace, A. F. Stein, and V. Pai, "Single-shot x-ray differential phase-contrast and diffraction imaging using two-dimensional transmission gratings," Opt. Lett. **35**(12), 1932–1934 (2010).
18. F. Pfeiffer, M. Bech, O. Bunk, P. Kraft, E. F. Eikenberry, C. Brönnimann, C. Grünzweig, and C. David, "Hard-X-ray dark-field imaging using a grating interferometer," Nat. Mater. **7**(2), 134–137 (2008).
19. S. W. Wilkins, T. E. Gureyev, D. C. Gao, A. Pogany, and A. W. Stevenson, "Phase-contrast imaging using polychromatic hard X-rays," (1996).
20. T. Dos Santos Rolo, S. Reich, D. Karpov, S. Gasilov, D. Kunka, E. Fohtung, T. Baumbach, and A. Plech, "A shack-hartmann sensor for single-shot multi-contrast imaging with hard x-rays," Appl. Sci. **8**(5), 737 (2018).
21. K. S. Morgan, P. Modregger, S. C. Irvine, S. Rutishauser, V. A. Guzenko, M. Stampanoni, and C. David, "A sensitive x-ray phase contrast technique for rapid imaging using a single phase grid analyzer," Opt. Lett. **38**(22), 4605–4608 (2013).
22. I. Zanette, T. Zhou, A. Burvall, U. Lundström, D. H. Larsson, M. Zdora, P. Thibault, F. Pfeiffer, and H. M. Hertz, "Speckle-based x-ray phase-contrast and dark-field imaging with a laboratory source," Phys. Rev. Lett. **112**(25), 253903 (2014).
23. M. Stampanoni, F. Marone, P. Modregger, B. Pinzer, T. Thüring, J. Vila-Comamala, C. David, and R. Mokso, "Tomographic Hard X-ray Phase Contrast Micro- and Nano-imaging at TOMCAT," *AIP Conf. Proc.* **1266**, 13–17 (2010).
24. P. Diemoz, P. Coan, C. Glaser, and A. Bravin, "Absorption, refraction and scattering in analyzer-based imaging: comparison of different algorithms," Opt. Express **18**(4), 3494–3509 (2010).
25. P. Diemoz, A. Bravin, and P. Coan, "Theoretical comparison of three X-ray phase-contrast imaging techniques: Propagation-based imaging, analyzer-based imaging and grating interferometry," Opt. Express **20**(3), 2789–2805 (2012).
26. F. A. Vittoria, G. K. N. Kallon, D. Basta, P. C. Diemoz, I. K. Robinson, A. Olivo, and M. Endrizzi, "Beam tracking approach for single-shot retrieval of absorption, refraction, and dark-field signals with laboratory x-ray sources," Appl. Phys. Lett. **106**(22), 224102 (2015).
27. A. Olivo and R. Speller, "A coded-aperture technique allowing x-ray phase contrast imaging with conventional sources," Appl. Phys. Lett. **91**(7), 074106 (2007).
28. P. Suortti, S. Fiedler, A. Bravin, T. Brochard, M. Mattenet, M. Renier, P. Spanne, W. Thomlinson, A. M. Charvet, H. Elleaume, C. Schulze-Briese, and A. C. Thompson, "Fixed-exit monochromator for computed tomography with synchrotron radiation at energies 18–90kev," J. Synchrotron Radiat. **7**(5), 340–347 (2000).
29. A. Mittone, I. Manakov, L. Broche, C. Jarnias, P. Coan, and A. Bravin, "Characterization of a sCMOS-based high-resolution imaging system," J. Synchrotron Radiat. **24**(6), 1226–1236 (2017).
30. A. Mittone, F. Baldacci, A. Bravin, E. Brun, F. Delaire, C. Ferrero, S. Gasilov, N. Freud, J. Létang, D. Sarrut, F. Smekens, and P. Coan, "An efficient numerical tool for dose deposition prediction applied to synchrotron medical imaging and radiation therapy," J. Synchrotron Radiat. **20**(5), 785–792 (2013).
31. P. C. Diemoz, C. K. Hagen, M. Endrizzi, and A. Olivo, "Sensitivity of laboratory based implementations of edge illumination X-ray phase-contrast imaging," Appl. Phys. Lett. **103**(24), 244104 (2013).
32. M. Endrizzi, F. A. Vittoria, G. Kallon, D. Basta, P. C. Diemoz, A. Vincenzi, P. Delogu, R. Bellazzini, and A. Olivo, "Achromatic approach to phase-based multi-modal imaging with conventional x-ray sources," Opt. Express **23**(12), 16473 (2015).
33. E. Knudsen, A. Prodi, J. Baltser, M. Thomsen, P. Willendrup, M. Sánchez del Río, C. Ferrero, E. Farhi, K. Haldrup, A. Vickery, R. Feidenhans'l, K. Mortensen, M. Nielsen, H. Poulsen, S. Schmidt, and K. Lefmann, "Mcxtrace: A monte carlo software package for simulating x-ray optics, beamlines and experiments," J. Appl. Crystallogr. **46**(3), 679–696 (2013).
34. T. P. Millard, M. Endrizzi, P. C. Diemoz, C. K. Hagen, and A. Olivo, "Monte Carlo model of a polychromatic laboratory based edge illumination x-ray phase contrast system," Rev. Sci. Instrum. **85**(5), 053702 (2014).
35. E. U. Ekpo, A. C. Hoban, and M. F. McEntee, "Optimisation of direct digital chest radiography using cu filtration," Radiography **20**(4), 346–350 (2014). Special Issue: Radiation Dose and Image Quality.

Optics EXPRESS

36. M. Endrizzi, A. Astolfo, F. A. Vittoria, T. P. Millard, and A. Olivo, "Asymmetric masks for laboratory-based X-ray phase-contrast imaging with edge illumination," Sci. Rep. **6**(1), 25466 (2016).
37. P. C. Diemoz and A. Olivo, "On the origin of contrast in edge illumination x-ray phase-contrast imaging," Opt. Express **22**(23), 28199–28214 (2014).